日本磁気学会
ISSN 2432-0250
Journal of the Magnetics Society of Japan
Electronic Journal URL: https://www.jstage.jst.go.jp/browse/msjmag

# Vol.49 No.3　2025

# Journal

# JOURNAL OF THE MAGNETICS SOCIETY OF JAPAN

Vol.49 No.3 2025

日本磁気学会

ISSN 2432-0250

HP: http://www.magnetics.jp/ e-mail: msj@bj.wakwak.com

Electronic Journal: http://www.jstage.jst.go.jp/browse/msjmag

TOEI

# TPM-2-08s25

## HcJの3σ/Ave. 0.2%[※1]を実現

## 渦電流補正方法[※2]も確立済

試料測定磁界
max 15Tesla

最大試料直径
10mm

## パルス励磁型磁気特性測定装置

永久磁石および磁性体粉末を固形化した高磁化試料のヒステリシス曲線の自動測定および描画、SPD（Singuler Point Detection）測定が可能です。（RT～+200℃）

※1　電気学会資料 MAG-18-088 参照

※2　電気学会資料 MAG-07-011 参照

## NdFeB(sintered) 測定例

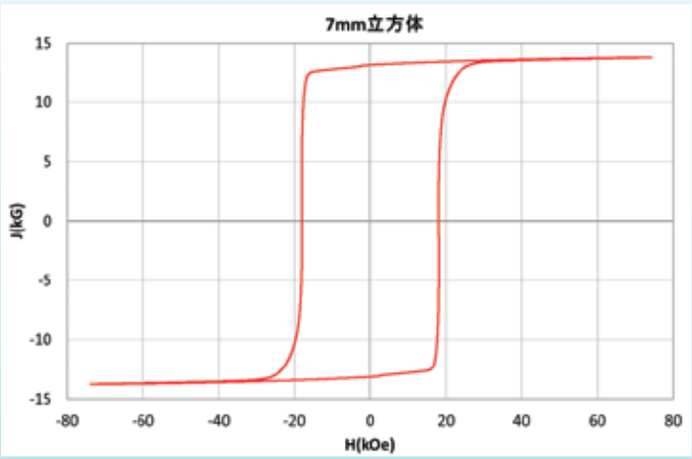


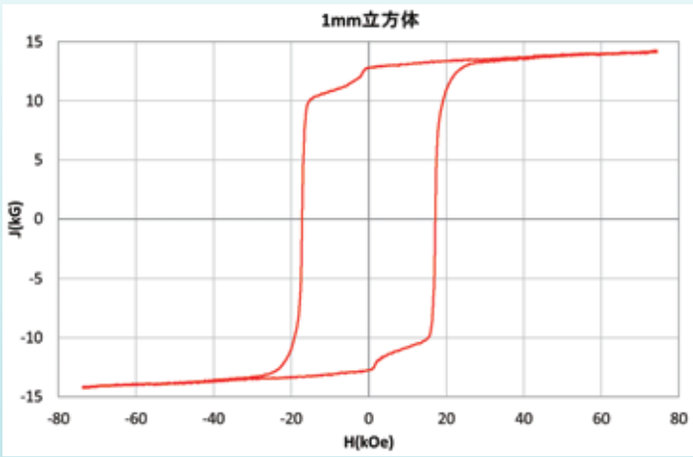


1mm 立方体測定用検出コイルはオプション品です

東英工業では他に振動試料型磁力計(VSM)、直流自記磁束計(JIS C2501 準拠)を始め、

各種磁気測定装置を取り揃えております。ぜひお問い合わせ下さい

TOEI 東英工業株式会社
http://www.toeikogyo.co.jp

〒194-0035 東京都町田市忠生1-8-13
TEL：042-791-1211 FAX：042-792-0490
E-mail：sales@toeikogyo.co.jp

# Journal of the Magnetics Society of Japan
## Vol. 49, No. 3

Electronic Journal URL: https://www.jstage.jst.go.jp/browse/msjmag


## CONTENTS

J. Magn. Soc. Jpn., **49**, 37-41 (2025) <Paper>

# Formation of high-density surface spin-wave soliton train

T. Iwata, T. Eguchi, and K. Sekiguchi*

Graduate School of Engineering Science, Yokohama National Univ., *Tokiwadai 79-5, Yokohama 240-8501, Japan*

*Faculty of Engineering, Yokohama National Univ., *Tokiwadai 79-5, Yokohama 240-8501, Japan*

The propagation characteristics of solitary spin waves in an yttrium iron garnet waveguide were investigated using a vector network analyzer and a real-time oscilloscope. Frequency- and time-domain analyses of spin-wave waveforms revealed the transition from linear to nonlinear response regimes and identified the threshold excitation power required to establish a single spin-wave soliton. With sufficiently high excitation power, a single spin-wave soliton transformed into a stable soliton train when the excitation frequency was modulated within dipole gaps. The frequency characteristics of the soliton train varied with the duration of the excitation power signal. The different time segments of the waveforms suggested the presence of new spin-wave modes excited through the self-modulation instability process, providing valuable insights into the formation of high-density spin-wave soliton trains.

**Keywords:** magnonics, spin-wave soliton train, nonlinear dynamics, modulational instability, magnetic insulator, microwave technique

## 1. Introduction

Spin waves, as a stream of angular momentum, induce no electric Joule heating, eliminating the need for charge flow [1)–4)]. This unique property facilitates ultra-low power information processing, making spin waves a promising candidate for next-generation information carriers. They enable a new class of devices, including magnon transistors [3)], magnon logic gates [5)–8)], magnon multiplexers [9),10)], magnon half-adders [11)], and spin-wave reservoirs [12)–15)]. However, practical magnetic materials like ferromagnetic permalloy, single-crystal iron, and even ferrimagnetic yttrium iron garnet (YIG) can introduce damping and distort the initial waveforms of spin waves due to finite dispersion and wave confinement. To overcome these challenges, spin-wave solitons have emerged as a potential solution.

Spin-wave soliton is generated when the Lighthill criterion, $DN < 0$, is satisfied. Here, $D = \partial^2\omega/\partial k^2$ is the dispersion parameter, $N = \partial\omega/\partial|u|^2$ is the nonlinear parameter [16)–22)], $\omega$, $u$, and $k$ represent spin-wave angular frequency, spin-wave amplitude, and wave vector, respectively. Previous soliton experiments have primarily focused on the backward volume magnetostatic spin wave (BVMSW) due to its analytically derived convex downward dispersion curve ($D > 0$) and negative nonlinear coefficient ($N < 0$) [20)–24)], or the forward volume magnetostatic spin wave (FVMSW) due to $D < 0$ and $N > 0$ [25)–27)], both of which fulfill the Lighthill criterion. Additionally, by leveraging modulational instabilities (MI) including induced modulational instability (IMI), coupled modulational instability (CMI) with two modulation continuous spin waves, and self-modulation instability (SMI) with a single spin-wave packet, pioneering research has demonstrated that spin-wave solitons can transform into a distinctive "train"-like signal pattern, characterized by consecutive multiple solitons [17),23)–25)].

While magnetostatic surface spin waves (MSSWs) do not inherently support spin-wave solitons due to their dispersion properties ($D < 0$, $N < 0$), recent research on soliton trains suggests that manipulating the carrier frequency around the dipole gap can alter the dispersion parameter ($D$), potentially enabling MSSW soliton formation [17)]. The dipole gap, a characteristic feature in the dispersion relation of spin waves, refers to an energy gap between two distinct branches of spin wave modes [27)–29)]. This gap arises due to the confinement effect in the thickness direction, which discretizes the dispersion curves when spins are pinned at the surface or interface of a magnetic material. Since no spin-wave states exist within the dipole gap, the input signal cannot be transmitted via spin waves within that frequency range, thereby manifesting as a dip in the transmission loss curve. The dipole gap plays a crucial role in soliton formation. Under conditions where both the spin-wave wave vector and the effective magnetic field are relatively small, the group velocity derived from the dispersion relation of magnetostatic waves indicates that MSSW soliton trains exhibit higher group velocities than BVMSW soliton trains [29)–32)], suggesting faster propagation compared to previously reported BVMSW soliton trains [24)].

In this paper, time-domain analysis of propagating spin waves spectroscopy was employed to investigate the propagation characteristics of MSSWs in both linear and nonlinear excitation power regimes. The position of the dipole gaps was determined by measuring the transmission loss curve using a vector network analyzer. By varying the excitation frequency around these dipole gaps, we observed the formation of MSSW solitons at specific frequencies and confirmed that self-modulation instability (SMI) could induce MSSW soliton trains. The density of the soliton train was controlled by adjusting the duration of the input excitation signal.

## 2. Experimental methods

Figure 1 illustrates the experimental setup. An yttrium iron garnet (YIG) film deposited on a gallium gadolinium garnet (GGG)

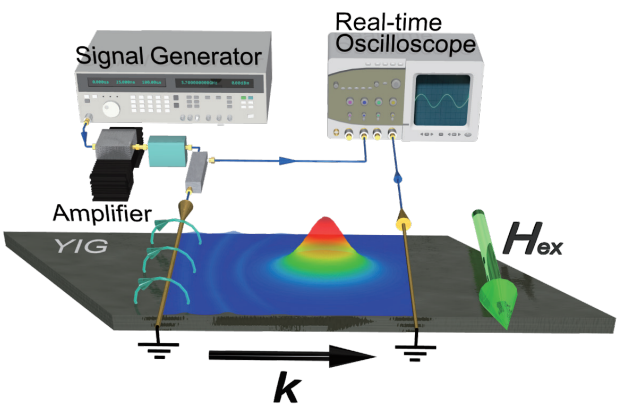


**Fig. 1.** Experimental setup for MSSW soliton generation. Signal generator provided input signal, which was amplified to 3W before being applied to excitation antenna. Output spin-wave signal was detected using real-time oscilloscope.

Corresponding author:
K. Sekiguchi (e-mail: sekiguchi-koji-gb@ynu.ac.jp).

substrate served as the waveguide. The YIG film dimensions were 10 μm thick, 2 mm wide, and 20 mm long. To minimize spin-wave boundary reflections, both ends of the waveguide were cut at a 45° angle. An external magnetic field was applied perpendicular to the waveguide to excite magnetostatic surface spin waves (MSSWs). The excitation and detection antennas were microstrip lines with widths of 450 μm and 75 μm, respectively, and a characteristic impedance of $Z_0 = 50\ \Omega$. The distance between the excitation and detection antennas was $d = 5$ mm. Time-domain measurements were conducted to observe the formation of spin-wave soliton trains. A signal generator produced a sinusoidal wave with a frequency ($f_{in}$) and a duration ($T_0$). A 3W RF amplifier amplified the input power to induce nonlinear effects on MSSWs. The output signal was captured by a real-time oscilloscope.

## 3. Results and discussion

### 3.1 Propagation of MSSWs

To establish a baseline for subsequent nonlinear studies, we first examined the linear response of our waveguide. The propagation characteristics of magnetostatic surface spin waves (MSSWs) were analyzed using a vector network analyzer (VNA). The input microwave power was set to a relatively low 5 dBm to avoid VNA receiver saturation and ensure linear spin-wave behavior. Figure 2 shows the transmission loss curve ($\Delta S_{21}$) in response to the external magnetic field ($H_{ex}$). The resonant frequencies ($f_{res}$) are determined as the maxima indicated by solid triangles. As shown in the inset of Fig. 2, the resonant frequencies ($f_{res}$) show a shift towards higher frequencies with larger $H_{ex}$. The dashed curve represents a theoretical fitting curve using the MSSW dispersion relation [29)–31)]. The fitting parameters are gyromagnetic ratio $\gamma = 1.76 \times 10^{11}$ T$^{-1}$ s$^{-1}$, permeability of vacuum $\mu_0 = 4\pi \times 10^{-7}$ H/m, saturation magnetization $M_s = 139.3$ kA/m, wave vector $k = 6795$ rad/m, and film thickness $L = 10$ μm. As shown, the experimentally observed $f_{res}$ agree well with the theoretical dispersion curve, confirming the propagation of MSSWs.

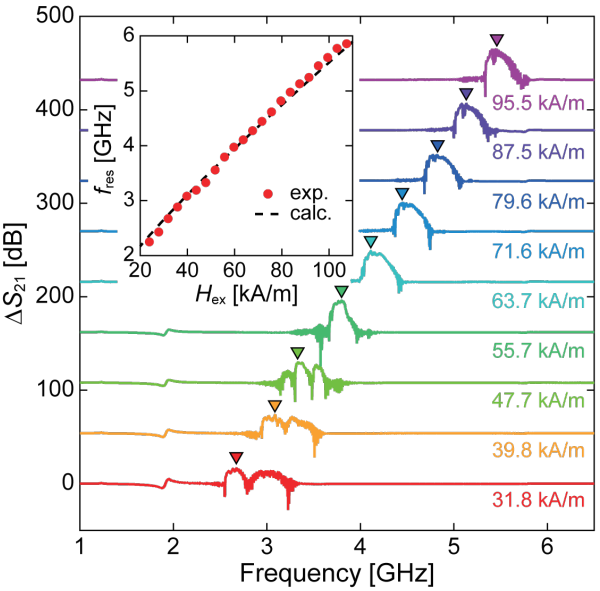


**Fig. 2.** Measured transmission spectra ($\Delta S_{21}$) of magnetostatic surface spin waves (MSSWs) propagating between microstrip lines spaced 5 mm apart. Inset shows experimentally determined resonance frequencies ($f_{res}$) as function of applied external magnetic field ($H_{ex}$). Dashed curve represents theoretical fit based on MSSW dispersion relation.

### 3.2 Formation of a single soliton

Figure 3(a) shows the time-domain signals of propagating spin waves at $H_{ex} = 95.49$ kA/m, at $f_{in} = 5.323$ GHz, and with $T_0 = 50$ ns. The origin of time ($t = 0$ ns) was defined at the rising edge of the input pulse. Accordingly, the excitation signal was applied during 0 ns $< t <$ 50 ns. To investigate nonlinear responses, we varied the input excitation power $P_{in}$ and measured the spin-wave signal $V_{SW}$, which was then converted to spin-wave power ($P_{SW} = {V_{SW}}^2/Z_0$). As shown in Fig. 3(a), the maximum values (peaks) of the spin waves are observed at approximately $t = 150$ ns for all input power levels ($P_{in}$). This arrival time of MSSWs is shorter than that of BVMSW solitons reported in the previous study [24)], indicating their faster propagation. With increasing excitation power, the peak value of the spin-wave signal increases, and the waveform becomes narrower. At $P_{in} = 222$ mW, the signal shape becomes the steepest, suggesting the possible formation of a spin-wave soliton.

To verify soliton formation, the peak power and full width at half maximum (FWHM) of the spin-wave signals were analyzed. Figure 3(b) shows the peak powers (represented by closed red circles) and FWHM values (represented by closed blue circles) of the spin-wave power at various input powers ($P_{in}$). Error bars are derived from the standard deviation of twenty measurements. As illustrated in Fig. 3(b), at lower input powers ($P_{in} < 41.3$ mW), the spin-wave power increases proportionally, as indicated by the fitting dashed line. However, as the input power increases ($P_{in} > 41.3$ mW), the output power demonstrates a more rapid increase, deviating from this proportional relationship. This nonlinear behavior is a hallmark of spin-wave solitons, as reported in previous studies [20),23),24),26)]. At the highest input power ($P_{in} = 222$ mW), the peak spin-wave power reaches 443 μW. This suggests that the threshold for soliton formation is located at $P_{in} = 41.3$ mW, where nonlinear response emerges.

Soliton formation was also confirmed by analyzing the FWHM. At lower input powers ($P_{in} < 85.0$ mW), the FWHMs gradually decrease from 27.3 ns to 23.2 ns. However, at $P_{in} = 85.0$ mW, there is a sudden drop in the FWHM from 23.2 ns to 13.3 ns. For $P_{in} > 85.0$ mW, the change in FWHM exhibits a gradual decrease from 13.3 ns to 7.19 ns. It is important to note that the spin-wave power possesses a 50 ns tail originating from the excitation duration, which affects the Gaussian fitting used to evaluate the FWHM, resulting in lower accuracy compared to that of the peak height. Therefore, we determine the threshold between the linear and nonlinear regimes of MSSW response as $P_{th} = 41.3$ mW, and the shaded area ($P_{in} > P_{th}$) indicates the nonlinear regime.

To gain insights into the nonlinear regime, we performed Fast Fourier Transform (FFT) analysis on the spin-wave signals ($V_{SW}$). As shown in Fig. 3(c), at lower power levels, the frequency spectra all show a single peak corresponding to the input frequency $f_{in} =$ 5.323 GHz, as represented by a vertical dashed line. As the input power $P_{in}$ increases and exceeds the threshold power ($P_{in} > 41.3$ mW), the FFT amplitudes at both ends of the spectra increase (indicated by arrows). At even higher power levels ($P_{in} > 136$ mW), the spectra split into multiple peaks. This phenomenon indicates spin-wave energy (i.e., frequency) transfer in the nonlinear regime through magnon-magnon scatterings. Specifically, this can be attributed to four-magnon scattering, where two magnons in the initial state $(k_0, f_0)$ transition into states $(k_+, f_+)$ and $(k_-, f_-)$, satisfying both energy conservation ($2f_0 = f_+ + f_-$) and momentum conservation ($2k_0 = k_+ + k_-$) [33)].

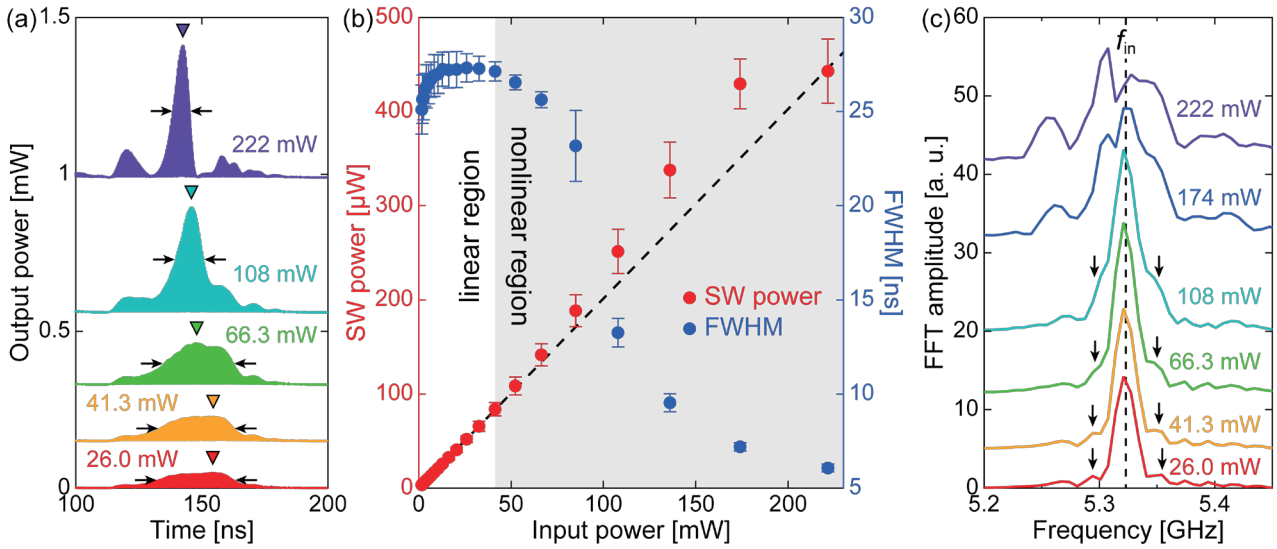


**Fig. 3.** Formation of single MSSW soliton. (a) Output power of propagating MSSWs as function of time with varying input power. (b) Peak power and full width at half maximum (FWHM) of spin-wave spectrum as function of input power. Dashed line represents linear contribution observed at low input power levels. (c) Amplitude spectra obtained by performing Fast Fourier Transform (FFT) on output spin-wave signals for different input power levels. Vertical dashed line indicates position of input frequency ($f_{in} = 5.323$ GHz).

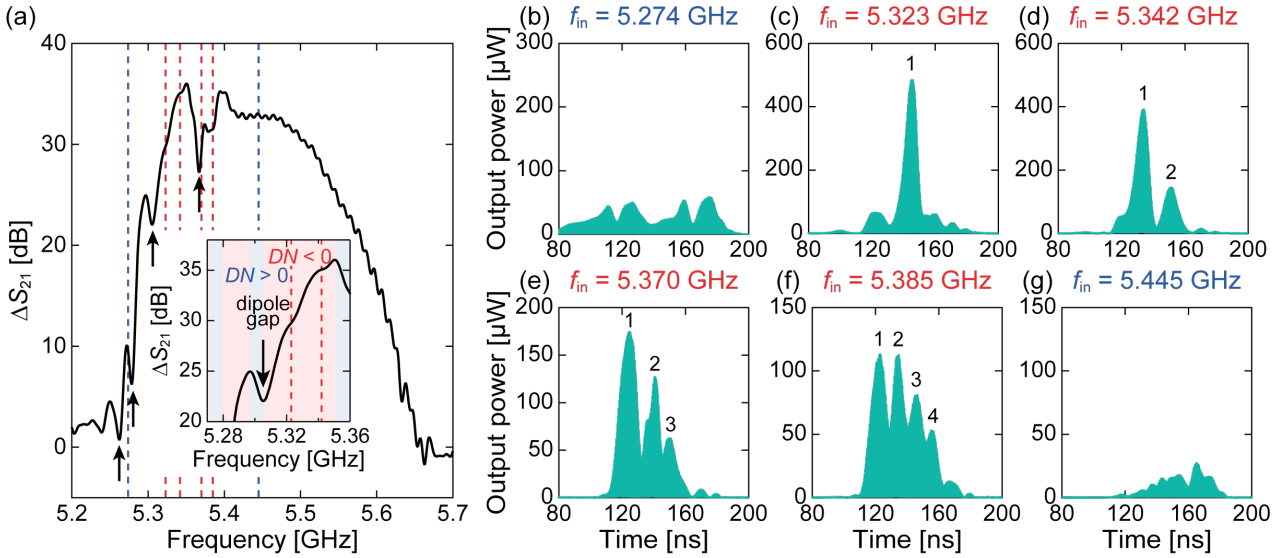


**Fig. 4.** Observation of dipole gaps and formation of MSSW soliton trains. (a) Transmission loss spectrum ($\Delta S_{21}$) measured at external magnetic field of $H_{ex} = 95.49$ kA/m, showing characteristic peaks and dips (indicated by arrows). (b)-(g) Time-domain waveforms of output spin-wave signals for various input frequencies at excitation power of $P_{in} = 174$ mW. Waveforms for frequencies on left-hand side of dipole gaps (indicated by blue vertical dashed lines) are shown in (b) and (g). Waveforms for frequencies on right-hand side (indicated by red vertical dashed lines) are shown in (c), (d), (e), and (f).

### 3.3 Formation of soliton trains

To determine the frequency positions of dipole gaps, the transmission loss curve ($\Delta S_{21}$) was measured using a VNA at 5.20 GHz $< f_{in} <$ 5.70 GHz. The input power of the VNA was fixed at 5 dBm. As shown in Fig. 4(a), the dipole gaps appear as dips on the transmission spectrum because they represent frequency ranges where the spin wave dispersion relation exhibits a significant change due to the presence of pinned spins at the surface. As indicated in the inset of Fig. 4(a), dispersion parameter $D < 0$ on the left-hand side (blue shaded regions) and $D > 0$ on the right-hand side (red shaded regions) of the dipole gaps, therefore $DN > 0$ on the left-hand side and $DN < 0$ on the right-hand side of the dips on the transmission spectrum. Soliton train formation experiments were conducted at various input frequencies near the dipole gaps, specifically at $f_{in} = 5.274$ GHz, 5.323 GHz, 5.342 GHz, 5.370 GHz, 5.385 GHz, and 5.445 GHz, with an excitation input power $P_{in} = 174$ mW, which exceeds the threshold power for the nonlinear regime.

Figures 4(b)-(g) illustrate the real-time output waveforms at these frequencies. On the positive slope sides of the dipole gaps [Figs. 4(c): $f_{in} = 5.323$ GHz, 4(d): $f_{in} = 5.342$ GHz, 4(e): $f_{in} = 5.370$ GHz, and 4(f): $f_{in} = 5.385$ GHz], indicated by the

vertical red dashed lines in Fig. 4(a), the outputs display stable waveforms with sharp peaks, characteristic of soliton trains. Observable patterns of 2-, 3-, and 4-peak soliton trains are shown in Figs. 4(d), 4(e), and 4(f), respectively. However, on the negative slope side of the dipole gaps [Figs. 4(b): $f_{in} = 5.274$ GHz and 4(g): $f_{in} = 5.445$ GHz], indicated by the vertical blue dashed lines in Fig. 4(a), the characteristic steep soliton waveforms are not observed in the waveforms. This demonstrates the occurrence of self-modulation instability (SMI) in MSSWs and highlights how the attractive/repulsive characteristics of spin waves vary depending on the positions of dipole gaps and the Lighthill criterion.

### 3.4 High-density soliton trains

Finally, we investigated the dependence of soliton train formation on the excitation duration. At an input frequency of $f_{in} = 5.385$ GHz and an input power of $P_{in} = 174$ mW, where the 4-peak soliton train shown in Fig. 4(f) was formed, we varied the duration ($T_0$) of the input excitation signal and analyzed the resulting waveforms. A waveform with $T_0 = 100$ ns is exemplified in Fig. 5(a). The black open circles indicate the positions of each peak (coach) of the soliton train, revealing eight peaks. Figure 5(b) illustrates the waveforms as the signal duration ($T_0$) is varied. Intriguingly, as $T_0$ increases, both the length of the output waveforms and the number of coaches increase. Moreover, we identified three distinct time-domain regions exhibiting different responses to changes in $T_0$. In the red-shaded region in Fig. 5(b) (referred to as the "front"), the number of coaches remained unchanged despite variations in $T_0$. In the green ("middle") and blue ("rear") shaded regions, the number of coaches changed. Notably, the "middle" region, where the waveforms exhibit no peaks, was observed exclusively for durations $T_0 \geq 150$ ns. The boundary between the "front" and "middle" regions remained constant at $t = 170$ ns, while the boundary between the "middle" and "rear" regions shifted linearly with increasing $T_0$. In other words, only within approximately 70 ns from the beginning of the input signal ("front") and approximately 85 ns before the end of the input signal ("rear") did the waveforms exhibit oscillations and form train-like patterns with multiple peaks.

Figure 5(c) shows the analysis of the number of coaches ($n_c$) as a function of $T_0$. The "total" data represents the total number of coaches in the waveforms. In the "front" and "middle" region, $n_c$ remains constant at $n_c = 5$ and $n_c = 0$, respectively. However, in the "rear" region, the $n_c$ increases as $T_0$ increases. Since the $n_c$ values of the "front" and "middle" regions remain constant, the behavior of $n_c$ of the "rear" region is reflected in that of the "total" region. When $T_0 \geq 150$ ns, $n_c$ of the "total" region saturates at $n_c = 14$. Figure 5(d) represents the time interval between coaches ($\Delta t_c$) as a function of $T_0$. In a similar manner to Fig. 5(c),

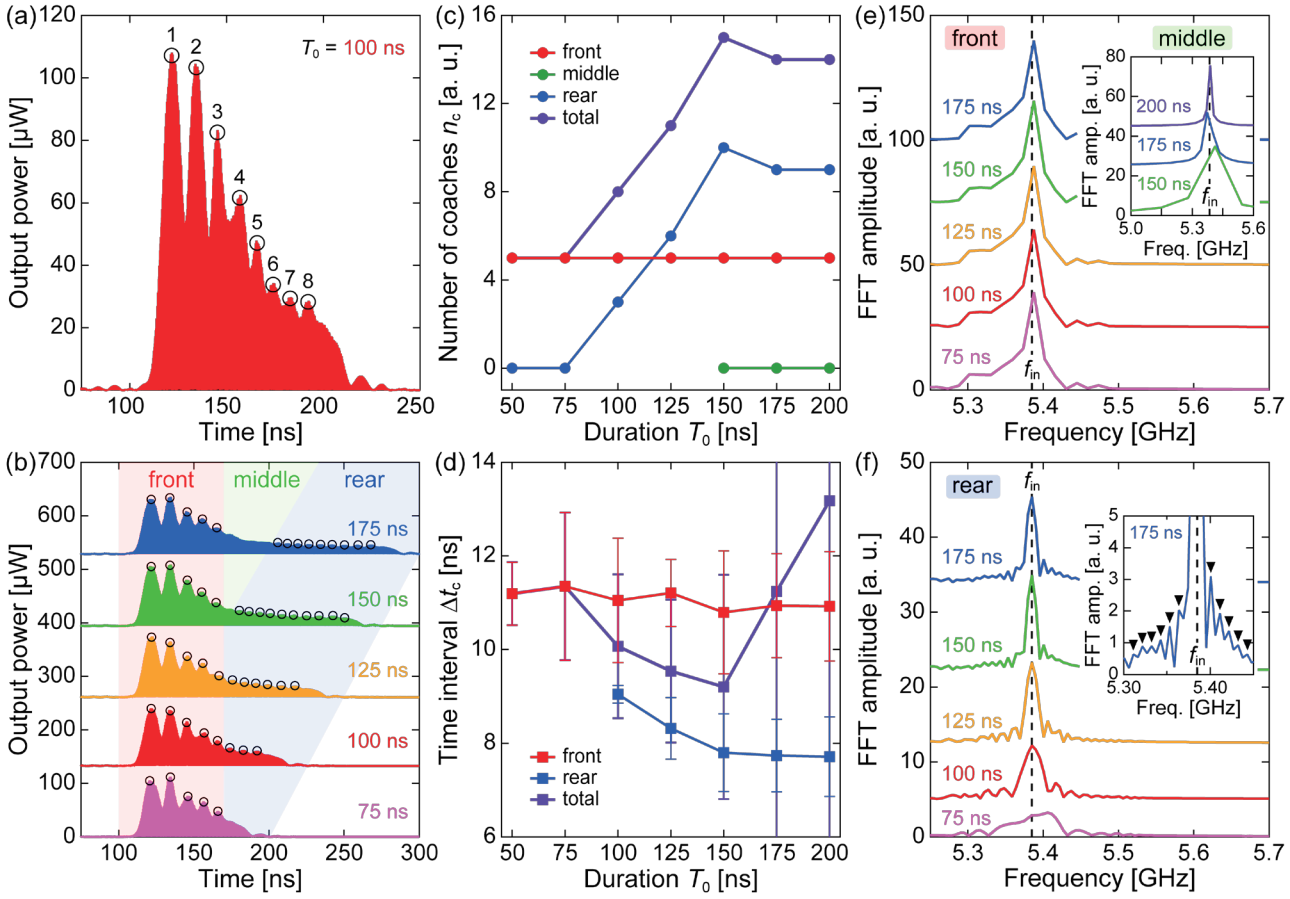


**Fig. 5.** Dependence of MSSW soliton trains on input signal duration. (a) Output waveform (converted to power) for input signal duration of $T_0 = 100$ ns. Black open circles indicate peaks (coaches) of soliton train. (b) Variation of output waveforms with changing $T_0$. Shaded regions indicate different time domains: "front" (red), "middle" (green), and "rear" (blue). (c) Number of coaches in soliton trains as function of $T_0$. (d) Time interval between coaches in soliton trains as function of $T_0$. (e) FFT amplitudes of "front" and "middle" regions. (f) FFT amplitude of "rear" region, with inset showing enlarged view at $T_0 = 150$ ns.

the analysis is divided into the "front," "rear," and "total" parts. $\Delta t_c$ is determined as the average of the time intervals between two neighboring coaches in each time region, with the error bars representing the standard deviation of $(n_c - 1)$ time intervals. It should be noted that the $\Delta t_c$ values of the "middle" region and of the "rear" region for $T_0 < 100$ ns are not defined since $n_c = 0$. $\Delta t_c$ of the "front" region remains approximately constant at $\Delta t_c = 11$ ns, whereas that of the "rear" region monotonically decreases and saturates at $\Delta t_c = 7.7$ ns as $T_0$ increases. Consequently, for $T_0 < 150$ ns, the $\Delta t_c$ of the "total" region also decreases, dragged by the decrease in the "rear" region. However, for $T_0 \geq 150$ ns, it rapidly increases due to the extension of the "middle" region. This suggests that the density of soliton trains is improved with the extension of the "rear" region, while it is reduced due to the extension of the "middle" region.

Figure 5(e) shows the frequency spectra of the "front" (100 ns $< t <$ 170 ns) and "middle" (170 ns $< t < t_{mr}$, where $t_{mr}$ is the time of the minimum just before the first coach of the "rear" region) parts. The FFT amplitudes in the "middle" region, defined only for $T_0 \geq 150$ ns, are shown in the inset. The vertical dashed line represents the input frequency $f_{in} = 5.385$ GHz. In the "front" region, the spectra do not change significantly with varying $T_0$, although the broadening of the spectrum is mainly attributed to lower frequencies compared to the spectra in the linear regime as shown in Fig. 3(c). The spin-wave spectra in the "middle" region show a single peak, suggesting similar spectral characteristics to a spin wave in the linear regime. Note that when the length of the "middle" region is small, especially at $T_0 = 150$ ns, the frequency resolution is low, which leads to an FFT spectrum with reduced clarity and precision.

Figure 5(f) shows the frequency spectra of the "rear" region. To ensure consistent data length, the FFT was performed within a unified time window of 190 ns: 170 ns $< t <$ 360 ns for $T_0 < 150$ ns, and $t_{mr} < t < t_{mr} + 190$ ns for $T_0 \geq 150$ ns. With an increase in $T_0$, the spectrum near $f_{in}$ becomes steeper and exhibits a comb-like shape. The inset depicts an enlarged view of the spectrum at $T_0 = 175$ ns. The black closed triangles represent the positions of side peaks of $f_{in}$, indicating the excitation of new SMI modes. Although the exact mechanism for the emergence of new SMI is currently unclear, a similar phenomenon of new-mode excitation has been reported in previous studies [17),25)]. In our experiments, the SMI could be induced by system noise or fluctuations in excitation power, since the spin waves in the "front" and "rear" regions are easily affected by the drastic variations in the rising and falling edges of the excitation signal. Power modulation of the excitation may induce SMI, and this scenario is consistent with the existence of the "middle" region where no spin wave soliton coaches were observed.

## 4. Conclusion

We investigated the propagation of magnetostatic surface spin waves (MSSWs) in an yttrium iron garnet waveguide, confirming their linear propagation characteristics using a vector network analyzer. By modulating the input frequency, we generated soliton trains in the nonlinear regime of a single MSSW soliton. The formation of stable soliton trains with multiple distinct peaks was found to occur precisely at frequencies corresponding to dipole gaps, satisfying the Lighthill criterion. We further analyzed the dependence of soliton trains on input signal duration, identifying three distinct time regions with varying characteristics. Extending the "rear" region led to a higher density of soliton trains. Fast Fourier Transform analysis revealed the excitation of new spin-wave modes due to nonlinear effects and self-modulation instability. Our findings demonstrate the potential for encoding and high-density information transfer using spin-wave soliton trains.

**Acknowledgements** This work was supported by Grants-in-Aid for Scientific Research (19H00861, 18H05346, and 22K18321) from the Japan Society for the Promotion of Science (JSPS). K. S. acknowledges the support of Grants-in-Aid for Scientific Research (20H05652).

## References

1) A. Barman *et al.*: *J. Phys.: Condens. Matter*, **33**, 413001 (2021).
2) A. V. Chumak *et al.*: *Nat. Phys.*, **11**, 453 (2015).
3) A. V. Chumak, A. A. Serga, and B. Hillebrands: *Nat. Commun.*, **5**, 4700 (2014).
4) A. V. Chumak *et al.*: *IEEE Trans. Magn.*, **58**, 0800172 (2022).
5) G. Talmelli *et al.*: *Sci. Adv.*, **6**, eabb4042 (2020).
6) M. P. Kostylev *et al.*: *Appl. Phys. Lett.*, **87**, 153501 (2005).
7) N. Kanazawa *et al.*: *Sci. Rep. A.*, **7**, 7898 (2017).
8) R. Hayashi, S. Nezu, and K. Sekiguchi: *Phys. Rev. Applied*, **22**, 034037 (2024).
9) K. Vogt *et al.*: *Nat. Commun.*, **5**, 3727 (2014).
10) Q. Wang, A. V. Chumak, and P. Pirro: *Nat. Commun.*, **12**, 2636 (2021).
11) Q Wang *et al.*: *Nat. Electron.*, **3**, 765-774 (2020).
12) R. Nakane, G. Tanaka, and A. Hirose: *IEEE Access*, **6**, 4462 (2018).
13) S. Watt and M. Kostylev: *Phys. Rev. Applied*, **13**, 034057 (2020).
14) S. Watt, M. Kostylev, and A. B. Ustinov: *J. Appl. Phys.*, **129**, 044902 (2021).
15) S. Nagase, S. Nezu, and K. Sekiguchi: *Phys. Rev. Applied*, **22**, 024072 (2024).
16) M. J. Lighthill: *IMA J. Appl. Math.*, **1**, 3 (1965).
17) M. Wu, B. A. Kalinikos, and C. E. Patton: *Phys. Rev. Lett.*, **93**, 157207 (2004).
18) A. N. Slavin: *Phys. Rev. Lett.*, **77**, 4644 (1996).
19) J. M. Nash *et al.*: *J. Appl. Phys.*, **83**, 2689 (1998).
20) M. Chen *et al.*: *Phys. Rev. B*, **49**, 12773 (1994).
21) N. G. Kovshikov *et al.*: *Phys. Rev. B*, **54**, 15210 (1996).
22) A. N. Slavin *et al.*: *Chaos*, **13**, 693 (2003).
23) M. Kawase, M. Iwaba, and K. Sekiguchi: *Jpn. J. Appl. Phys.*, **59**, SEED01 (2020).
24) T. Eguchi, M. Kawase, and K. Sekiguchi: *Appl. Phys. Express*, **15**, 083001 (2022).
25) M. Wu and B. A. Kalinikos: *Phys. Rev. Lett.*, **101**, 027206 (2008).
26) P. De Gasperis, R. Marcelli, and G. Miccoli: *Phys. Rev. Lett.*, **59**, 481 (1987).
27) B. A. Kalinikos, N. G. Kovshikov, and A. N. Slavin: *Zh. Eksp. Teor. Fiz.*, **94**, 159 (1988).
28) B. A. Kalinikos: *Sov. Phys. J.*, **24**, 718 (1981).
29) B. A. Kalinikos and A. N. Slavin: *J. Phys. C: Solid State Phys.*, **19**, 7013 (1986).
30) K. Y. Guslienko, R. W. Chantrell, and A. N. Slavin: *Phys. Rev. B*, **68**, 024422 (2003).
31) R. W. Damon and J. R. Eshbach: *J. Phys. Chem. Solids*, **19**, 308 (1961).
32) T. Eguchi *et al.*: *Phys. Rev. Research*, **4**, 033135 (2022).
33) G. T. Kazakov, A. V. Kozhevnikov, and Y. A. Filimonov: *Phys. Solid State*, **39**, 288 (1997).

**Received Oct. 18, 2024; Accepted Feb. 14, 2025**

J. Magn. Soc. Jpn., **49**, 42-46 (2025) <Paper>

# Chaotic vortex dynamics in circular magnetic nanodisk with double disk structure induced by AC magnetic field

K. Horizumi, T. Chiba*,**, and T. Komine

Graduate School of Science and Engineering, Ibaraki Univ., *Hitachi, Ibaraki, 316-8511, Japan*
*Frontier Research Institute for Interdisciplinary Science (FRIS), Tohoku Univ., *Sendai, Miyagi 980-8578, Japan*
**Depertment of Applied Physics, Graduate School of Engineering, Tohoku Univ., *Sendai, Miyagi 980-8578, Japan*

Generating chaos in spintronics devices has attracted much attention for the application of physical reservoir computing. We theoretically investigate the influence of the potential deformation due to the nanodisk structure on the magnetic vortex core dynamics in circular magnetic nanodisk. Considering a circular magnetic nanodisk with an additional disk, we numerically calculate the magnetic vortex dynamics using the Thiele equation. The deformation potential is modeled by using micromagnetic simulation. The chaos is induced by applying an AC magnetic field to the nanodisk with only an additional disk. In contrast, chaos disappears when the AC magnetic field is applied to a nanodisk without an additional disk.

**Keywords:** vortex dynamics, Thiele equation, chaos, nonlinear potential

## 1. Introduction

In recent years, physical reservoir computing has been actively studied for machine learning of time series data in physical systems[1]. In general, it has been reported that the learning performance improves close to the border between a stable and an unstable (chaotic) dynamics region [2, 3], which is the so-called "*edge of chaos*."

Spintronics devices are one of the leading candidates for physical reservoirs[4, 5]. In fact, it has been reported that the short-term memory capacity, one of the indicators of learning performance, actually improved at the edge of chaos when a spin-torque nano oscillator with a two-free-layer structure was used[6]. It has been experimentally confirmed that chaos can be generated in vortex spin torque oscillator (VSTO) using nanocontacts[7, 8], random pulse input[9], and feedback circuits[10]. However, no report exists that only an alternating-current (AC) magnetic field can generate chaos in VSTOs.

This study investigates whether chaos can be generated by applying only an AC magnetic field to nanodisk. Here the nanodisk is intended to be used as a free layer in VSTO. We theoretically demonstrate the generation of chaos by using the relatively minor modification of the additional disk to the nanodisk.

## 2. Calculation model

Figure 1 shows the calculation model of a circular magnetic nanodisk with an additional disk. We consider a circular magnetic nanodisk with an additional disk. The additional disk has the same material as the nanodisk but with a smaller radius than the nanodisk as shown in Fig. 1. In this paper, the coordinate system is a Cartesian coordinate system with the origin at the center of the nanodisk. The basis vector is denoted as $\boldsymbol{e}_k$ $(k = x, y, z)$. When an AC magnetic field $h_x = h_0 \sin(2\pi f t)$ is applied in the $x$-axis direction as an external force, the motion of the magnetic vortex core can be described by the following the Thiele equation[11, 12],

$$-G\boldsymbol{e}_z \times \dot{\boldsymbol{X}} - |D|(1+\xi s^2)\dot{\boldsymbol{X}} - \frac{\partial W}{\partial \boldsymbol{X}} - c\mu^* \boldsymbol{e}_z \times \boldsymbol{H} = \boldsymbol{0}, \qquad (1)$$

where $\boldsymbol{X} = (X, Y, 0)$ is the position vector of the magnetic vortex core, $\dot{\boldsymbol{X}}$ is the velocity vector, $s = \sqrt{X^2 + Y^2}$ is the distance of the magnetic vortex core from the center of the nanodisk, $W(s)$ is the potential function, $\boldsymbol{H} = (h_x, 0, 0)$ is the external magnetic field, $G = 2\pi pML/\gamma$ is the gyro-coefficient, $D = -(2\pi\alpha ML/\gamma)[1 - (1/2)\ln(R_0/R)]$ is the damping coefficient, $\mu^* = \pi MLR$ is the magnetic field coefficient, $M$ is the saturation magnetization, $\gamma$ is the gyromagnetic constant, $\alpha$ is the Gilbert damping constant, $R_0$ is the vortex core radius, $\xi$ is the nonlinear damping constant, $p$ is the polarity, and $c$ is the chirality of the magnetic vortex. The values of $M = 1300$ emu/cm$^3$, $\gamma = 1.764 \times 10^7$ rad/(Oe s), $\alpha = 0.01$, $R_0 = 10$ nm, $\xi = 2$, $p = 1$, and $c = 1$ were used for each parameter[9, 13]. Here, FeB is assumed as the nanodisk material. The nanodisk has the radius $R$ of 187.5 nm and the thickness $L$ of 5 nm, and the additional disk has the radius $R_a$ of 20 nm or 40 nm. The thickness of the additional disk was 1/3 of that of the nanodisk.

As the above-mentioned definitions of the parameters, the parameters $G$ and $D$ are generally dependent on the thickness $L$. If an additional disk is present, it is thought that the parameters$G$and $D$ depend on the normalized distances $s$ through the thickness dependence. However, in this study, the parameters $G$ and $D$ are treated as

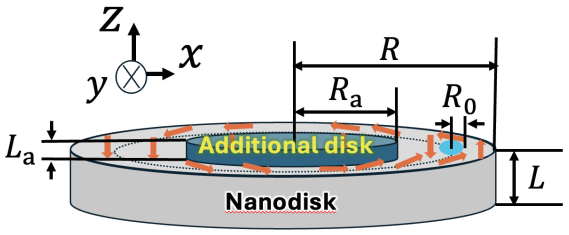


**Fig.1** Schematic illustration of the circular magnetic nanodisk with an additional disk.

Corresponding author: T. Komine (e-mail: takashi.komine.nfm@vc.ibaraki.ac.jp).

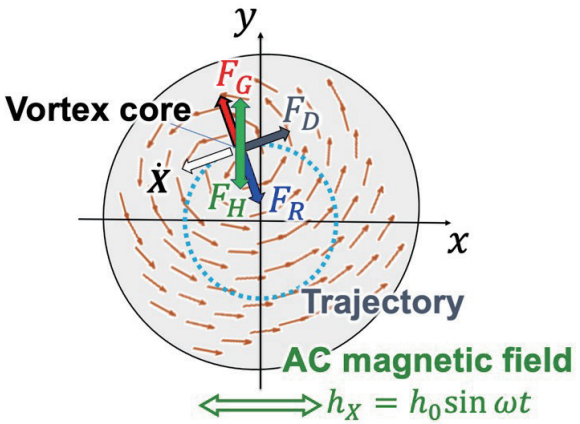


**Fig. 2** Schematic illustration of vortex core dynamics driven by magnetic forces.

independent of the normalized distances. This assumption is justified by the fact that the variation in $L$ is negligible. Because the effect of the modified potential is adequate even if the parameters are independent of the normalized distance s, the results presented in this paper are primarily qualitative rather than quantitative.

Each term in the Thiele equation described by equation (1) denotes a gyro-term $\boldsymbol{F}_{\mathrm{G}}$, a damping term $\boldsymbol{F}_{\mathrm{D}}$, a restoring force $\boldsymbol{F}_{\mathrm{R}}$, and a force due to the magnetic field $\boldsymbol{F}_{\mathrm{H}}$, respectively. The effects acting on the magnetic vortex core are schematically shown in Fig. 2. The additional disk on the nanodisk modifies the potential shape, which is incorporated into the Thiele equation as a restoring force $\boldsymbol{F}_{\mathrm{R}} = -\partial W/\partial \boldsymbol{X}$. The potential shape $W(s)$ for the vortex core is obtained by changing the position of the vortex core describing two vortex ansatz (TVA)[13], assuming that the magnetizations of the nanodisk and the additional disk are rigid and strongly coupled by exchange coupling. The potential, the sum of the magnetostatic and exchange energies, is calculated using micromagnetics calculation.

The magnetic vortex core motion was investigated by numerically solving the Thiele equation for various AC magnetic field amplitudes $h_0$ and the frequencies $f$.

### 3. Result and discussion

Figures 3(a), (b), and (c) show the bird's view of potentials of magnetic vortex core on the nanodisk

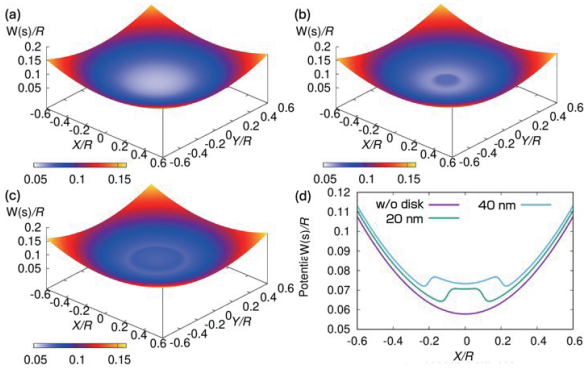


**Fig. 3** Potentials of vortex core for on the nanodisk (a) without additional disk, (b) with 20nm-radius additional disk, and (c) with 40nm-radius additional disk. (d) Potentials along the diameter direction.

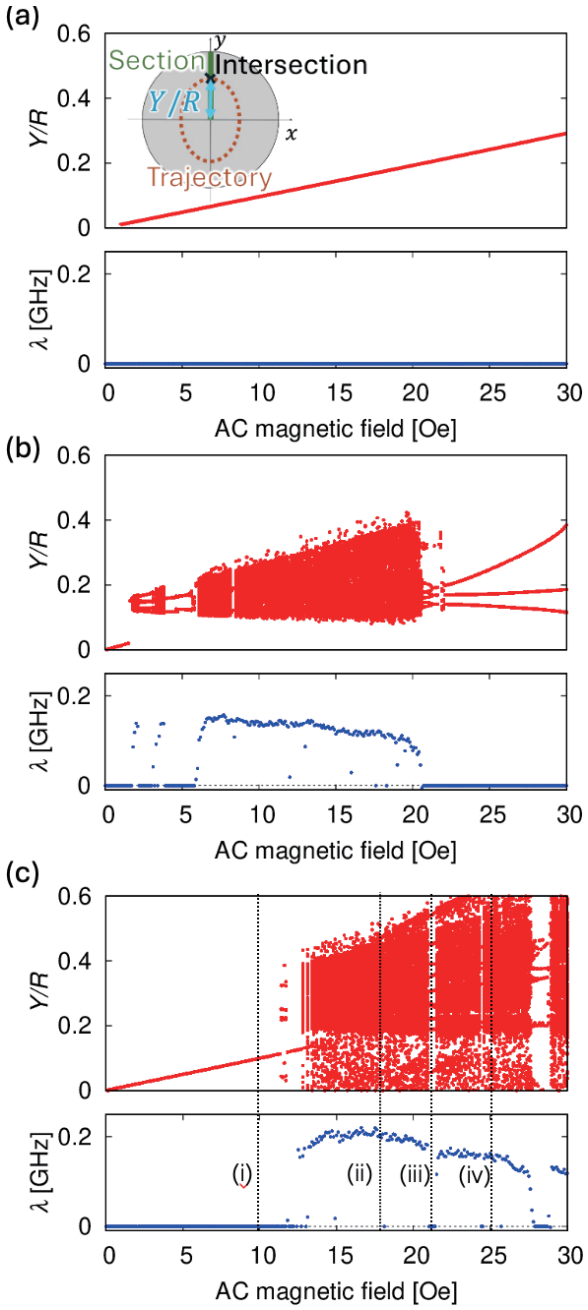


**Fig. 4** Lyapunov exponent and Poincaré section when an AC magnetic field with a frequency of 100 MHz was applied to a nanodisk (a) without additional disk, (b) with 20 nm-radius additional disk, and (c) with 40 nm-radius additional disk. The AC magnetic field amplitude was varied from 0 to 30 Oe. (a) Inset shows a schematic illustration of the definition of Poincaré section.

without an additional disk, with an additional disk of radius $R_{\mathrm{a}} = 20$ nm, and with an additional disk of radius $R_{\mathrm{a}} = 40$ nm, respectively. Figure 3(d) also shows the potentials along the diameter direction across the center. The potential on the nanodisk without an additional disk shows almost the harmonic potential described by the quadratic functions of the distance $s$ from the center. If there is an additional disk, the potential has local

minimums near the additional disk edge. This is because the potential is harmonic when the magnetic vortex core exists within the additional disk, while the magnetic vortex core is trapped at the boundary of the additional disk due to magnetostatic energy. When the vortex cores are located outside the additional disk, the harmonic potential is almost identical to that without the additional disk.

The Lyapunov exponent and Poincaré section are indices that determine whether the behavior of a solution in a dynamical system is chaotic or not[14]. The Lyapunov exponent indicates the initial value sensitivity and a general characteristic of chaos. The Lyapunov exponent is an index calculated as the degree of increase or decrease in the difference between two solutions that are slightly different at a certain time. If the sign of the Lyapunov exponent is positive, the dynamics may show chaotic behavior. Also, when the Lyapunov exponent is zero, the orbit of the vortex core is a limit cycle. Generally, the Lyapunov exponent $\lambda$ for an AC-applied system is calculated for the autonomous system[15]. An autonomous system means a system whose equations do not depend explicitly on time $t$. Introducing the new third component as $Z = \omega t$, the Thiele equation is rewritten as an autonomous system.

$$\begin{pmatrix} \dot{X} \\ \dot{Y} \\ \dot{Z} \end{pmatrix} = A \begin{pmatrix} \dfrac{\partial W}{\partial s} \cdot \dfrac{X}{s} \\ \dfrac{\partial W}{\partial s} \cdot \dfrac{Y}{s} + c\mu^* h_0 \sin(Z) \\ \omega \end{pmatrix}, \quad (2)$$

$$A = \begin{pmatrix} -|D|(1+\xi s^2)/\Delta & -G/\Delta & 0 \\ G/\Delta & -|D|(1+\xi s^2)/\Delta & 0 \\ 0 & 0 & 1 \end{pmatrix}, \quad (3)$$

$$\Delta = \begin{vmatrix} -|D|(1+\xi s^2) & -G \\ G & -|D|(1+\xi s^2) \end{vmatrix}. \quad (4)$$

For a general three-dimensional autonomous system $\dot{\boldsymbol{U}} = f(\boldsymbol{U}), \boldsymbol{U} = {}^t(U_1, U_2, U_3)$, the Lyapunov exponent is defined as follows. At a certain time $t_0$, a solution $\boldsymbol{V^1}(t_0)$ is created that deviates slightly from the solution $\boldsymbol{U}(t_0)$. The difference between the two solutions of $\boldsymbol{U}(t_0)$ and $\boldsymbol{V^1}(t_0)$ is set to $\varepsilon$. If the solution deviates from the time $t_0$ by a certain time step $\Delta t$, we define $l_1$ expressed as

$$l_1 = \frac{\log(p_1)}{\Delta t}, p_1 = \frac{\left|\boldsymbol{V^1}(t_0 + \Delta t) - \boldsymbol{U}(t_0 + \Delta t)\right|}{\varepsilon}, \quad (5)$$

where the distance is defined by $|\boldsymbol{V} - \boldsymbol{U}| = \sqrt{\sum_{i=1}^{3}(V_i - U_i)^2}$. In order to calculate the Lyapunov exponent $\lambda$, $l_i$ added together an infinite number of times as follows.

$$\lambda = \lim_{n\to\infty} \sum_{i=1}^{n} l_i, p_i = \frac{\left|\boldsymbol{V^i}(t_0 + i\,\Delta t) - \boldsymbol{U}(t_0 + i\,\Delta t)\right|}{\varepsilon}, \quad (6)$$

where

$$\boldsymbol{V^i}(t_0 + i\,\Delta t) = \boldsymbol{U}(t_0 + (i-1)\,\Delta t) + \{\boldsymbol{V^{i-1}}(t_0 + (i-1)\,\Delta t) - \boldsymbol{U}(t_0 + (i-1)\,\Delta t)\}/p_{i-1}.$$

It means the normalization of the distance between the two solutions. In this calculation, the iteration number $n$ is the order of $10^6$, sufficient to saturate the Lyapunov exponent $\lambda$ in this system.

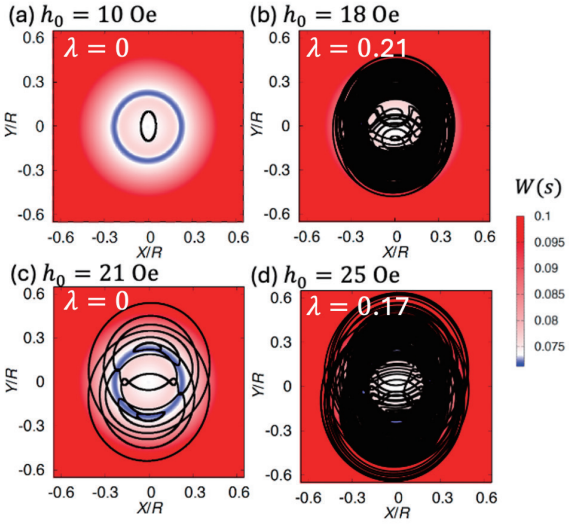


**Fig. 5** Phase diagram when an AC magnetic field with frequency of 100 MHz was applied to a nanodisk with 40 nm-radius additional disk. The AC magnetic field amplitudes were (a) 10 Oe, (b) 18 Oe, (c) 21 Oe, and (d) 25 Oe, respectively.

The Poincaré section is a plot of the intersection of a line segment from the origin with the trajectory of the magnetic vortex core in the $x-y$ plane during the vortex motion. In general, if the Lyapunov exponent is zero and the vortex core continues to follow the same orbit, that is, the limit cycle, the Poincaré section will have only a finite number of points. In particular, in the case of a limit cycle that describes an ellipse with a single period, the Poincaré section has only one point. Solutions with a positive Lyapunov exponent and chaotic behavior show a Poincaré section that fills the line segment for the intersection with the orbit. In this study, the Poincaré

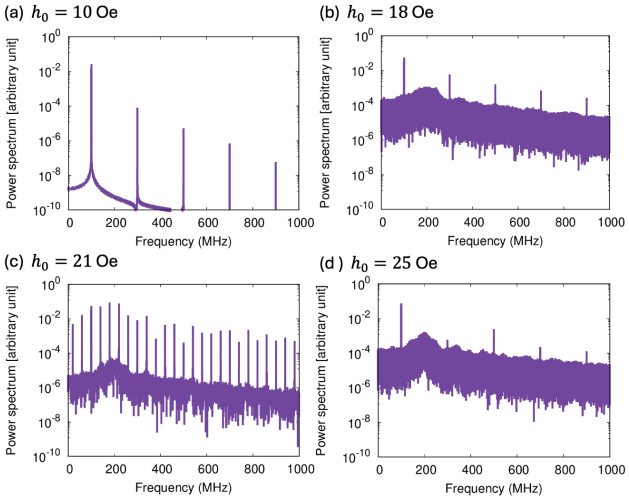


**Fig. 6** FFT of $X/R$ when an AC magnetic field with frequency of 100 MHz and amplitudes of (a) 10 Oe, (b) 18 Oe, (c) 21 Oe, and (d) 25 Oe was applied to a nanodisk with 40 nm-radius additional disk.

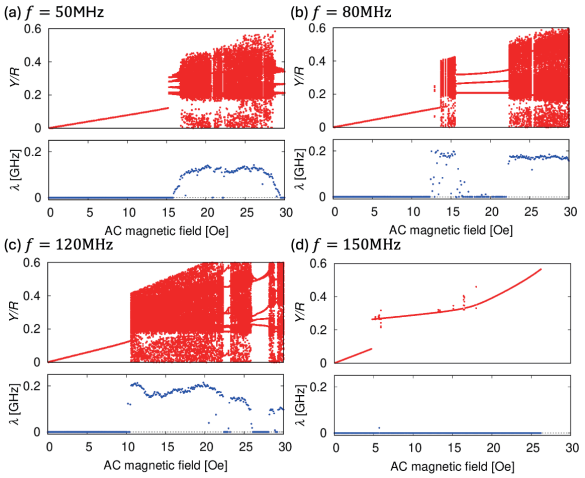


**Fig. 7** Lyapunov exponents and Poincaré sections for the nanodisk with an additional disk of radius 40 nm, where the amplitude of the external magnetic field is varied from 0 Oe to 30 Oe. The frequency of the external magnetic field is set to (a) 50 MHz, (b) 80 MHz, (c) 120 MHz, and (d) 150 MHz, respectively.

section is the intersection of the positive region of the $y-$axis and the orbit after entering the steady state.

The Lyapunov exponent $\lambda$ and the corresponding Poincaré sections are shown in Figs. 4 (a), (b), and (c) for the cases with and without the additional disk when the AC magnetic field of 100 MHz frequency is applied. The reason why we chose this value will be explained later. The amplitude of the AC field $h_0$ was varied from 0 to 30 Oe. Without the additional disk shown in Fig. 4 (a), the limit cycle has an elliptical shape stretched in the $y-$axis direction and the magnetic vortex core trajectory expands with the AC field amplitude, so the Poincaré section of the relative position $Y/R$ is a monotonically increasing. When there is an additional disk, as shown in Figs. 4 (b) or (c), in the small amplitude region, the Lyapunov exponent maintains zero, and the Poincaré section is still linear due to ordinal oscillatory motion. However, as the vibration radius increases, the Lyapunov exponent becomes positive, and the intersection points is proportional to the AC amplitude due to the additional disk. Thereafter, chaotic and non-chaotic regions appear alternately.

In the case of the 40 nm radius additional disk, the solution trajectories of the magnetic vortex core in the $x-y$ plane, the so-called phase diagram, are plotted in Figs. 5 (a), (b), (c), and (d) for amplitudes $h_0$ = (i) 10, (ii) 18, (iii) 21, and (iv) 25 Oe for an AC magnetic field of 100 MHz frequency. In the case of the magnetic field amplitude $h_0 = 10$ Oe shown in Fig. 5(a), the magnetic vortex core oscillates around the bottom of the harmonic potential formed by the additional disk. On the other hand, in the case of AC field amplitude of $h_0 = 18$ Oe as shown in Fig. 5(b), the magnetic vortex core repeatedly moves inside and outside the additional disk, indicating chaotic behavior rather than periodic oscillations. In the case of AC field amplitude $h_0 = 21$ Oe shown in Fig. 5 (c), a complex limit cycle is observed, which is different from the chaotic behavior. Furthermore, when the AC field amplitude $h_0 = 25$ Oe shown in Fig. 5 (d), the chaotic behavior appears again. These results are consistent with the Lyapunov exponent $\lambda$ shown in Fig. 4(c), suggesting that the system exhibits chaotic behavior at a certain AC field amplitude $h_0$.

The FFT power spectra of $X(t)$ for amplitudes of (a) 10 Oe, (b) 18 Oe, (c) 21 Oe, and (d) 25 Oe are shown in Fig. 6. When the amplitude of the AC magnetic field is 10 Oe, there is a steep peak at 100 MHz, the same frequency as that of the AC magnetic field. This is because the magnetic vortex has a rotational motion near the origin, resulting in a simple limit cycle of elliptical orbits. When the AC field amplitude is 18 Oe, the frequency spectrum unexpectedly becomes broader at the input signal frequency of 100 MHz. In contrast, when the amplitude is 21 Oe, the spectrum shows the discrete multimode with multiple superimposed frequencies. When the amplitude of the AC magnetic field is 25 Oe, the result is broad around the frequency of the input signal, as is the case with an amplitude of 18 Oe. Every case has peaks at an odd multiple of the AC magnetic field frequency of 100 MHz. It is because the damping and restoring force terms have nonlinearity associated with reduced distance $s$. In case of $h_0 = 10$ Oe as shown in Fig.6 (a), however, the oscillation is single mode due to the small oscillation radius and the effect of nonlinearity almost being so small.

Figure 7 shows the Lyapunov exponents and Poincaré sections of a 40 nm disk with AC magnetic field frequencies of (a) 50 MHz, (b) 80 MHz, (c) 120 MHz, and (d) 150 MHz, respectively. A chaos-induced region exists from 50-120 MHz, but in the case of 150 MHz, the Lyapunov exponent and Poincaré section show that chaos is almost not generated. This is thought to be due to the frequency of the AC magnetic field being close to the resonance frequency of the VSTO, which consists of the nanodisk as a free layer. The value is approximately 200 MHz. Therefore, it is suggested that the frequency needs to be adjusted for chaos to be induced. Also, in the case of frequencies that have the region induce chaos, some zones would be used as the edge of chaos, which is the intermedia between a stable state and chaos. Furthermore, above 150 MHz, there is no region available as an edge for chaos.

The chaos and complex limit cycles are caused by a reversal of the direction of the velocity vector $\boldsymbol{v}$ due to potential gradients. We consider the Thiele equation as below

$$\begin{pmatrix}\dot{X}\\ \dot{Y}\end{pmatrix} = \mathrm{A}\left[\frac{\partial W}{\partial s}\cdot\frac{1}{s}\cdot\begin{pmatrix}X\\ Y\end{pmatrix} + \begin{pmatrix}-Gc\mu^*\\ -|D|(1+\xi s^2)c\mu^*\end{pmatrix} h_0\sin(\omega t)\right], \quad (7)$$

$$\mathrm{A} = \frac{1}{G^2+|D|(1+\xi s^2)^2}\begin{pmatrix}-|D|(1+\xi s^2) & -G\\ G & -|D|(1+\xi s^2)\end{pmatrix}. \quad (8)$$

To simplify, we can rewrite the Thiele equation as

$$\boldsymbol{v} = \left(\frac{\partial W}{\partial s}\right)A'\boldsymbol{X} + A\boldsymbol{b}, \quad (9)$$

Where $\boldsymbol{v} = {}^{t}(\dot{X}, \dot{Y})$, $\boldsymbol{X} = {}^{t}(X, Y)$,

$$\boldsymbol{A}' = \frac{s^{-1}}{G^2 + |D|(1+\xi s^2)^2}\begin{pmatrix} -|D|(1+\xi s^2) & -G \\ G & -|D|(1+\xi s^2) \end{pmatrix}. \quad (10)$$

Furthermore, since $G^2 \gg D^2$, the off-diagonal elements of the matrix A are dominant, thus, a more straightforward expression is as follows

$$\boldsymbol{v} \approx \frac{\partial W}{\partial s}\begin{pmatrix} -Y \\ X \end{pmatrix} + A\boldsymbol{b}. \quad (11)$$

The direction of $\boldsymbol{v}$ is reversed obeying the sign of $\partial W/\partial s$. Therefore, the change in the potential shape due to the additional disk can induce chaos in the vortex core motion depending on the sign of the potential gradient.

These results suggest that VSTO with an additional disk, a simple modification, may improve learning performance when used as a physical reservoir because the edges of chaos are more pronounced.

## 4. Summary

In this study, the behavior of the magnetic vortex core was numerically investigated when an AC magnetic field was applied to a circular magnetic nanodisk with an additional disk. When the input AC magnetic field amplitude was varied from 0 to 30 Oe with the frequency of 100 MHz, no chaos was observed in the absence of an additional disk, but chaos was observed in the presence of an additional disk. In the case of the 40 nm disk, chaos was induced in some regions when the frequency of the external magnetic field was 50-120 MHz, but almost not at 150 MHz. This indicates that the amplitude and frequency must be adjusted to induce chaos in nanodisk with an additional disk. These results are justified by the Lyapunov exponent, Poincaré section, phase diagram, and FFT consistency. Therefore, the VSTO, which consists of the nanodisk as a free layer, may improve the machine learning performance.

**Acknowledgments** This work was partly supported by Grants-in-Aid for Scientific Research (Grants Nos. 24K00916, 24K06912, 24H00018, 22K14591, 22H01805) from the Japan Society for the Promotion of Science.

## References

1) D. Verstraeten, B. Schrauwen, M. D'Haene, D. Stroobandt: *Neural Netw*. 391 (2007).
2) J. Boedecker, O. Obst, J. T. Lizier *et al.*: *Theory Biosci.* **131,** 205 (2012).
3) N. Bertschinger and T. Natschläger: *Neural. Comput.* **16**, 1413 (2004).
4) J. Grollier, D. Querlioz, and M. D. Stiles: *Proc. IEEE* **104**, 2024 (2016).
5) J. Grollier *et al.*: *Nat. Electron*. **3,** 360 (2020).
6) T. Yamaguchi *et al.*: *Phys. Rev. B*, **107**, 054406 (2023).
7) S. Petit-Watelot *et al.*: *Nature Phys.,* **8**, 682 (2012).
8) T. Devolder *et al.*: *Phys. Rev. Lett.*, **123**, 147701 (2019).
9) Y. Imai *et al.*: *Sci. Rep*., **12**, 21651 (2022).
10) A. Kamimaki *et al.*: *Phys. Rev. Res*., **3**, 043216 (2021).
11) A. A. Thiele: *Phys. Rev. Lett.,* **30**, 230 (1973).
12) K. Y. Guslienko *et al.*: *Phys. Rev. Lett.* **96,** 067205 (2006).
13) A. Dussaux *et al.*: *Phys. Rev. B*, **86,** 014402 (2012).
14) S. Strogatz: Nonlinear Dynamics and Chaos: With Applications to Physics, Biology, Chemistry, and Engineering (CRC Press, 2018).
15) I. Shimada, and T. Nagashima: *Prog. Theor. Phys.* **61**, 1605 (1979).

**Received Oct. 29, 2024; Accepted Jun. 20, 2025**

**Erratum**

“Magnetic anisotropy of Sm(Fe-Co-Ni)$_{12}$-B thin films and formation of ThMn$_{12}$ phase by element substitution and addition”

Y. Mori, S. Nakatsuka, T. Sato, M. Doi, T. Shima

Journal of the Magnetics Society of Japan 2025 Volume 49 Issue 2 Pages 27-31
https://doi.org/10.3379/msjmag.2503R002

---

The original article contains typographical errors in the reference 15). The volume number and the article number should be “Appl. Sci., **12**, 4860 (2022)”, not “Appl. Sci., **10**, 6037 (2020)”. These errors have been corrected in the following PDF and online versions of J-STAGE.

J. Magn. Soc. Jpn., **49**, E1-E6 (2025) <Paper>

# Magnetic anisotropy of $Sm(Fe\text{-}Co\text{-}Ni)_{12}$-B thin films and formation of $ThMn_{12}$ phase by element substitution and addition

Y. Mori*†, S. Nakatsuka*, T. Sato**, M. Doi*, and T. Shima*
*Graduate School of Engineering, Tohoku Gakuin Univ., *Shimizukoji* , *Sendai 984-8588, Japan*
**Faculty of Engineering, Tohoku Gakuin Univ., *Shimizukoji* , *Sendai 984-8588, Japan*

The combined addition of Ni and Co is a promising method for stabilizing the $ThMn_{12}$-type crystal structure without significantly decreasing the saturation magnetization. In this work, the structure and magnetic properties of $Sm(Fe\text{-}Co)_{12}$-B thin films by substituting Ni and Co with a part of Fe sites and adding B were investigated in detail. It was observed that when the Fe sites of $Sm(Fe\text{-}Co\text{-}Ni)_{12}$ thin films were partially substituted with Ni, the peak intensity from the $ThMn_{12}$-type phase decreased, but recovered with increasing the amount of Co substitution. Furthermore, most of the samples with combined Ni and Co substitution had an isotropic or in-plane easy axis of magnetization with respect to the film plane. However, it was confirmed that the easy axis of magnetization was varied to the perpendicular direction by adding a small amount of B to the $Sm(Fe\text{-}Co\text{-}Ni)_{12}$ thin films.

**Keywords**: $ThMn_{12}$-type crystal structure, magnetic anisotropy, element substitution, $Sm(Fe\text{-}Co\text{-}Ni)_{12}$-B thin film

## 1. Introduction

$RFe_{12}$ (R: rare earth element) compounds (hereafter referred to as 1:12) with a tetragonal $ThMn_{12}$-type crystal structure are expected to have a high saturation magnetization due to their high Fe content, and they are promising candidates for new high-performance permanent magnet materials. In particular, it has been confirmed that $SmFe_{12}$-based compounds exhibit superior intrinsic magnetic properties at room temperature and at high temperatures compared with $Nd_2Fe_{14}B$ sintered magnets[1)-6)]. For example, the saturation magnetization ($\mu_0 M_s$ = 1.78 T), anisotropy field ($\mu_0 H_A$ = 12 T), and Curie temperature ($T_C$ = 879 K) can be obtained at room temperature in a $Sm(Fe_{0.8}Co_{0.2})_{12}$ thin film[1)]. Furthermore, it was reported that a high coercive force of 1.2 T was obtained in a B-doped Sm(Fe-Co)-B thin film prepared by sputtering, which is due to a columnar structure in which $Sm(Fe\text{-}Co)_{12}$ particles were surrounded by the grain boundary phase[7)]. In recent years, we have succeeded in further increasing the coercivity of $Sm(Fe\text{-}Co)_{12}$-B thin films through the grain boundary diffusion of nonmagnetic elements[8)-11)], and we reported that a particularly large coercivity ($\mu_0 H_c$ = 1.8 T) can be obtained by depositing an Al cap layer[11)]. However, in previous studies, it was well known that the $SmFe_{12}$ phase was thermodynamically unstable in the bulk state, and therefore it was necessary to substitute some of the Fe sites with stabilizing elements such as Al, Si, Ti, V, Co, and Zr[12)-14)]. The addition of these stabilizing elements inevitably results in a significant decrease in the saturation magnetization of the $SmFe_{12}$ compound, which has been a major drawback. Therefore, in order to obtain a sufficiently high saturation magnetization while maintaining the stability of $ThMn_{12}$-type compounds, it is necessary to either minimize the amount of stabilizing elements added or to replace part of the Fe sites with ferromagnetic elements that function as stabilizers.

Recently, Landa et al. reported using a fundamental framework based on density-functional theory in which $SmNi_4(Fe\text{-}Co)_8$ alloys exhibit a negative formation energy and that the formation energy is minimal when the mole fraction of Co in Fe-Co is 0.4[15)-16)]. To obtain a high saturation magnetization without affecting the

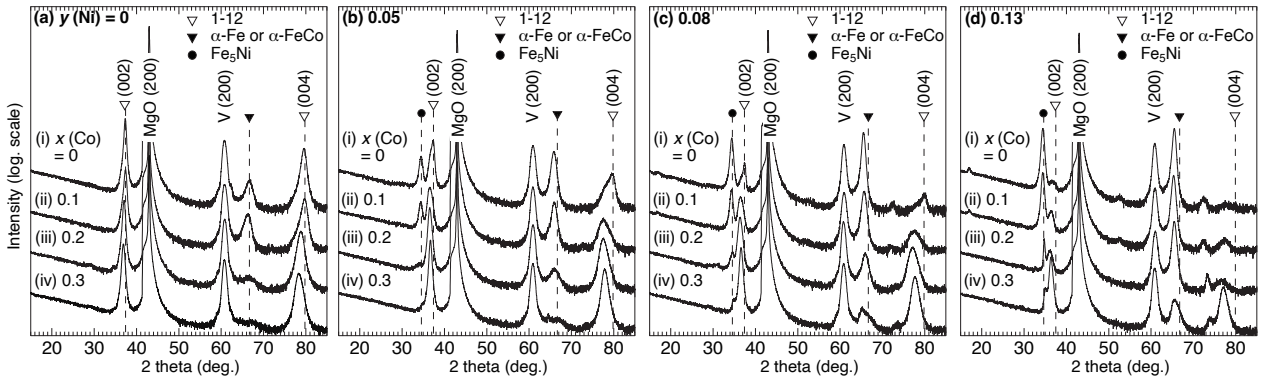


**Fig. 1.** Out-of-plane XRD patterns for $Sm(Fe_{1-x-y}Co_xNi_y)_{12}$ thin films with different amount of Ni substitution [(a) ~ (d)] and Co substitution [(i) ~ (iv)].

Corresponding author: Y. Mori (e-mail: s236532001@g.tohoku-gakuin.ac.jp).

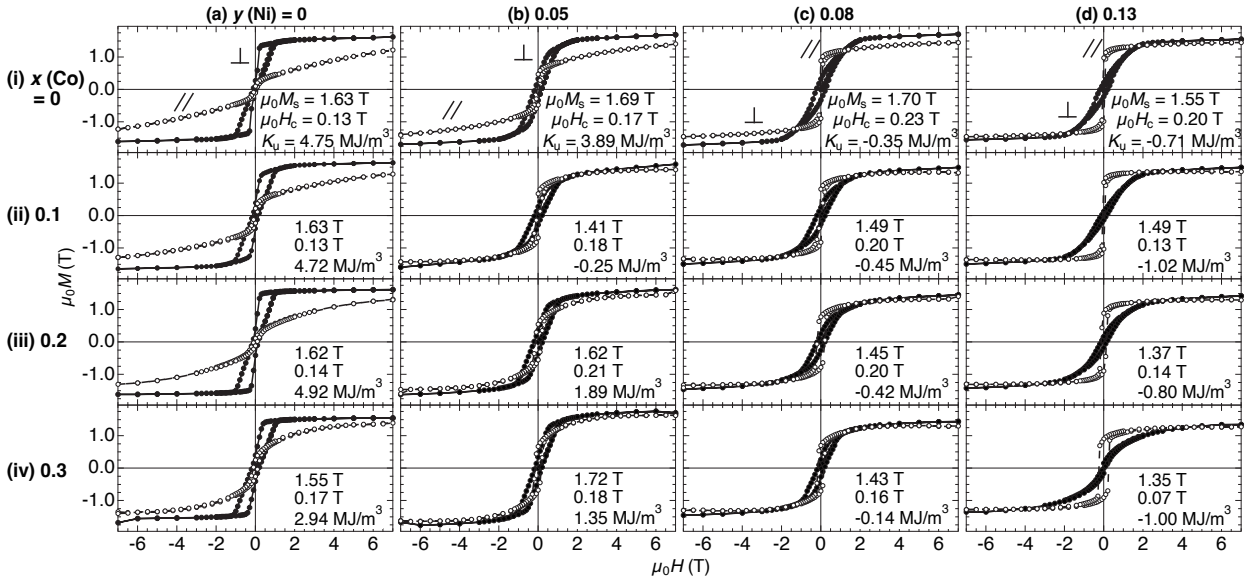


**Fig. 2.** Magnetization curves for $Sm(Fe_{1-x-y}Co_xNi_y)_{12}$ [$x$: (i) ~ (iv), $y$: (a) ~ (d)] thin films. Filled and open circles are denoted curves measured in perpendicular and parallel directions to the film plane, respectively.

anisotropy field or Curie temperature, they propose replacing a certain amount of Fe and Co with Ni in $Sm(Fe_{1-x}Co_x)_{12}$ alloys. Therefore, the simultaneous substitution of Ni and Co is expected to be a candidate method for stabilizing the $SmFe_{12}$ phase without significantly decreasing the saturation magnetization. In this study, $Sm(Fe\text{-}Co)_{12}$ and $Sm(Fe\text{-}Co)_{12}$-B thin films with added Ni, which is expected to stabilize the $ThMn_{12}$-type phase without significantly decreasing saturation magnetization, are prepared and the crystal structure and magnetic properties by variation of the film composition, such as the amount of Co and Ni substituted for Fe and the amount of B added are also investigated in detail.

## 2. Experimental procedure

The samples were prepared by using an ultra-high vacuum magnetron sputtering system with an ultimate pressure of less than $4.0 \times 10^{-7}$ Pa. First, a V buffer layer with a thickness of 20 nm was deposited on a MgO(100) single crystal substrate at a substrate temperature ($T_s$) of 400ºC in an Ar gas atmosphere with a process gas pressure of 0.17 Pa. Subsequently, a 50 nm of $Sm(Fe_{1-x-y}Co_xNi_y)_{12}$-B layer ($x$ = 0 ~ 0.5, $y$ = 0 ~ 0.13) was deposited by co-sputtering with Sm, Fe, $Fe_{50}Co_{50}$, $Fe_{80}B_{20}$ and Ni targets at $T_s$ = 400ºC. The mole fractions of Ni and Co ($x$, $y$) were determined from the results of energy dispersive X-ray analysis (EDX). However, due to the detection limit of light elements, the content of B cannot be determined by EDX, so the B content was determined by the ratio of the deposition rate of boron to that of the $Sm(Fe\text{-}Co\text{-}Ni)_{12}$-B layer. Finally, a 10-nm V cover layer was deposited as a protective layer to prevent oxidation at room temperature. The crystal structure was analyzed by X-ray diffraction (XRD) with Cu-$K_\alpha$ radiation by adjusting the $\chi$ and $\varphi$ angles to adopt out-of-plane and in-plane configurations. The magnetic properties were evaluated using a superconducting quantum interference device (SQUID) magnetometer. All measurements were performed at room temperature.

## 3. Results and discussion

XRD patterns for $Sm(Fe_{1-x-y}Co_xNi_y)_{12}$ thin films with different amounts of Co substitution ($x$ = 0 ~ 0.3) and Ni substitution ($y$ = 0 ~ 0.13) are shown in Fig. 1. As shown in Fig. 1(a)(i), the (002) and (004) peaks of the $ThMn_{12}$-type crystal structure were clearly observed in the Ni- and Co-unsubstituted $SmFe_{12}$ thin film. At Co substitution $x$ = 0.1, the position of the peak from the 1:12 phase remained almost unvaried, but it was confirmed that the peak position shifted to a lower angle with increasing $x$. It was confirmed that as the Ni substitution amount $y$ increased from (a) to (d), the peak intensity from the 1:12 phase decreased, while at the same time, the peak intensities from the $Fe_5Ni$ and α-Fe phases seen at 2θ = 34.6º and 66.6º increased. These results indicate that the substitution of Co into Fe sites elongates the lattice spacing of the $c$-plane, while the substitution of Ni inhibits the formation of the 1:12 phase and instead leads to the formation of $Fe_5Ni$ and α-Fe phases. In addition, in the $Sm(Fe\text{-}Co\text{-}Ni)_{12}$ thin film [(b)-(d)], the peak intensity from the 1:12 phase was recovered by increasing the Co substitution amount $x$, and the peaks of the $Fe_5Ni$ phase and the α-Fe phase were decreased, that is, their formation was suppressed. This suggests that the presence of Co facilitates the formation of the 1:12 phase with Ni added.

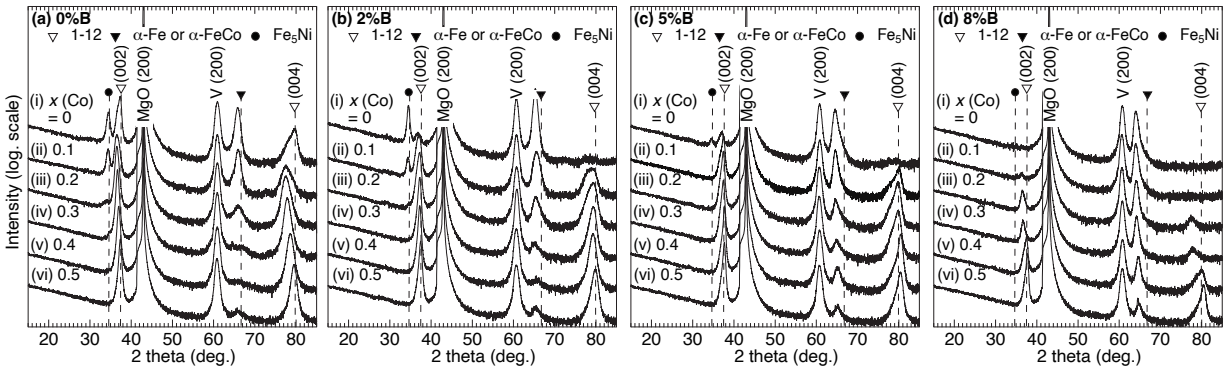


**Fig. 3.** XRD patterns for $Sm(Fe_{0.95-x}Co_xNi_{0.05})_{12}$-B thin films with different amount of B content [0 ~ 8% B: (a) ~ (d)] nd Co substitution [$x$: (i) ~ vi)].

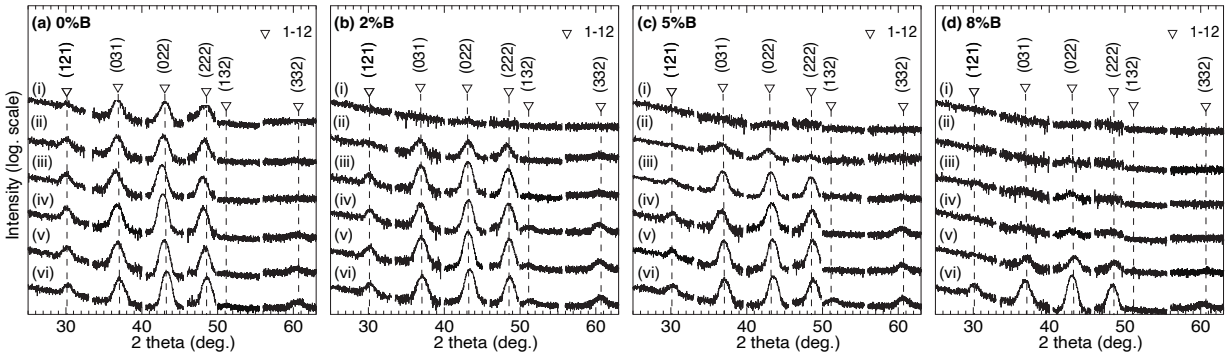


**Fig. 4.** In-plane XRD patterns for $Sm(Fe_{0.95-x}Co_xNi_{0.05})_{12}$-B thin films with different amount of B content [0 ~ 8% B: (a) ~ (d)] and Co substitution [$x$ = 0 ~ 0.5: (i) ~ (vi)].

Magnetization curves for $Sm(Fe_{1-x-y}Co_xNi_y)_{12}$ thin films with different amounts of Co ($x$) and Ni ($y$) substitution are shown in Fig. 2. The filled and open circles denote the results measured in perpendicular and parallel directions to the film plane, respectively. In the $SmFe_{12}$ thin film without Co or Ni substitution ($x$ = 0 and $y$ = 0) shown in Fig. 2(a)(i), a high saturation magnetization $\mu_0 M_s$ =1.63 T exhibiting perpendicular magnetic anisotropy was obtained. Increasing the Co substitution amount $x$ improved the squareness of the hysteresis loop in the first quadrant, but further increasing $x$ to 0.3 decreased the uniaxial magnetic anisotropy constant ($K_u$). The value of $K_u$ was calculated by subtracting the integral of the out-of-plane $M$-$H$ curve from the integral of the in-plane $M$-$H$ curve in the first quadrant. As shown in Fig. 2(b), when the Ni substitution amount $y$ was 0.05, it was confirmed that $K_u$ decreased due to Co substitution and the easy direction of magnetization varied from perpendicular to the film plane to almost isotropic. In addition, as shown in Fig. 2(c), when $y$ was increased to 0.08, the easy axis of magnetization of the $Sm(Fe\text{-}Ni)_{12}$ thin film varied from the perpendicular direction to the film plane to the in-plane direction. Furthermore, even when the amounts of Co substitution and Ni substitution were further increased, the easy axis of magnetization remained in-plane. Thus, it was confirmed that Ni substitution does not contribute to improve the hard magnetic properties of $Sm(Fe\text{-}Co)_{12}$ compounds, and that the in-plane magnetic anisotropy becomes predominant as the Ni content increases. Therefore, an attempt was made to improve the anisotropy by adding B to $Sm(Fe\text{-}Co\text{-}Ni)_{12}$ thin films with a small amount of Ni substitution $y$ = 0.05.

XRD patterns of $Sm(Fe_{0.95-x}Co_xNi_{0.05})_{12}$-B thin films prepared with different amounts of B content (B = 0 ~ 8%) and Co substitution ($x$ = 0 ~ 0.5) measured in the out-of-plane configuration ($\chi = \varphi = 0$) are shown in Fig. 3. It should be noted that the B content is determined by the deposition rate of boron during the deposition of the $Sm(Fe_{0.95-x}Co_xNi_{0.05})_{12}$-B layer. In the B-free $Sm(Fe\text{-}Co\text{-}Ni_{0.05})$ thin film shown in Fig. 3(a), it was observed that the (002) and (004) peak positions of the 1:12 phase shifted to lower angles when $x$ was 0.1, and then shifted to higher angles as $x$ increased further. On the other hand, when the amount of B added was increased to 2% and 5%, the peak intensity of the 1:12 phase decreased in the case of samples not substituted with Co, and when the amount of B added was further increased to 8% (d), it was confirmed that the peak of the 1:12 phase almost completely disappeared. However, the peak intensity of the 1:12 phase was increased significantly in the 2%B and 5%B films by substituting Co into the Fe site ($x$ = 0.1), and the peak intensity further increased with increasing $x$. In addition, it was confirmed that the peak intensity of the $Fe_5Ni$ and α-Fe

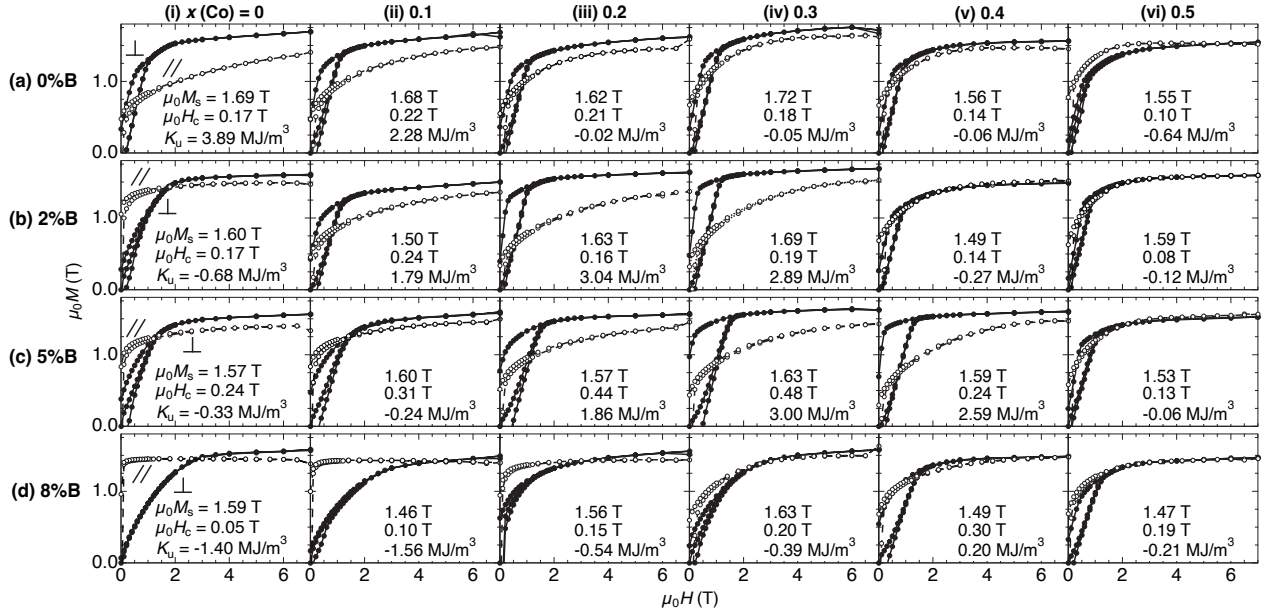


**Fig. 5.** Magnetization curves for $Sm(Fe_{0.95-x}Co_xNi_{0.05})_{12}$-B thin films with different amount of B content [0 ~ 8% B: (a) ~ (d)] and Co substitution [$x$: (i) ~ (vi)].

phases decreased with increasing Co substitution, suppressing their formation. In the 8%B sample, the peak intensity of the 1:12 phase recovered from 0.2 to 0.5 due to an increase in the Co substitution amount, but it was confirmed that the intensity was lower than that of the 5%B sample with a lower B addition at each $x$ value.

XRD patterns of $Sm(Fe_{0.95-x}Co_xNi_{0.05})_{12}$-B ($x$ = 0 ~ 0.5, B = 0 ~ 8%) thin films obtained from an in-plane configuration (various $\chi$ and $\varphi$ angles) are shown in Fig. 4. As shown in Fig. 4(a), the (121), (031), (022), and (222) peaks from the 1:12 phase were clearly observed in the $Sm(Fe_{0.95}Ni_{0.05})_{12}$ thin film without B addition. Similar to the results in Fig. 3(a), it was confirmed that the intensity of peaks from the 1:12 phase decreased with the addition of B, and its intensity was restored by increasing the amount of Co substitution. When increasing the Co substitution amount $x$, (132) and (332) superlattice reflections were also observed, and the Co substitution amounts at which these peaks began to be observed were $x$ = 0.4, 0.3, and 0.3 in the 0%B, 2%B, and 5%B samples, respectively. Furthermore, the peak intensities of the (132) and (332) peaks were stronger in the 2%B and 5%B samples compared with the sample without B addition. From the results shown so far, it was confirmed that increasing the amount of Co substitution and adding a small amount of B, such as 2%B or 5%B, promotes the formation of the Sm(Fe-Co-Ni)$_{12}$ phase.

Magnetization curves for $Sm(Fe_{0.95-x}Co_xNi_{0.05})_{12}$-B ($x$ = 0 ~ 0.5, B = 0 ~ 8%) thin films are shown in Fig. 5. As shown in Fig. 5(a), $K_u$ of the B-free Sm(Fe-Co-Ni)$_{12}$ thin film decreased with increasing Co substitution amount $x$ [(i)~(vi)], and it was confirmed that the easy axis of magnetization varied from perpendicular to the film plane to in-plane at $x$ = 0.5. In addition, as shown in Fig. 5(b), by adding 2%B, the easy axis of magnetization of the Co-unsubstituted Sm(Fe-Ni)$_{12}$-B thin film was in the film plane. However, $K_u$ increased as the amount of Co substitution increased up to $x$ of 0.2 and decreased with further increase in $x$. When the B content was 5% (c), $K_u$ similarly increased with Co substitution, reaching a maximum at $x$ = 0.3. In contract, when B was added in larger amounts up to 8%, the easy axis of magnetization could not be obtained in the direction perpendicular to the film plane at any Co substitution amount $x$. Thus, it was confirmed that the addition of B to the Sm(Fe-Co-Ni)$_{12}$ thin film increases the Co substitution amount ($x$), which exhibits perpendicular magnetic anisotropy.

Scatter plots of the axial ratio $c/a$ and the uniaxial magnetic anisotropy constant $K_u$ for $Sm(Fe_{0.95-x}Co_xNi_{0.05})_{12}$-B ($x$ = 0 ~ 0.5, B = 0 ~ 8%) thin films are shown in Fig. 6. The value of $c/a$ was obtained from the peak positions of the 1:12 phase in Figs. 3 and 4. For films without B, $c/a$ increased as $x$ increased up to 0.2 and then decreased with further increases in $x$. In the sample with 2% B addition, $c/a$ decreased as $x$ increased to 0.2, and at $x$ = 0.3, $c/a$ increased slightly, and a further increase in $x$ resulted in a slight decrease in $c/a$. At 5%B, $c/a$ decreased significantly with a Co substitution amount of $x$ = 0.1, but it then increased at $x$ = 0.2 and 0.3, and decreased slightly at 0.4. By adding 8%B, high $c/a$ values were confirmed at $x$ = 0.1 and 0.2, and these values decreased significantly with a further increase in B content. On the other hand, a high $K_u$ value of 3.89 MJ/m$^3$ was obtained for the $SmFe_{12}$ thin

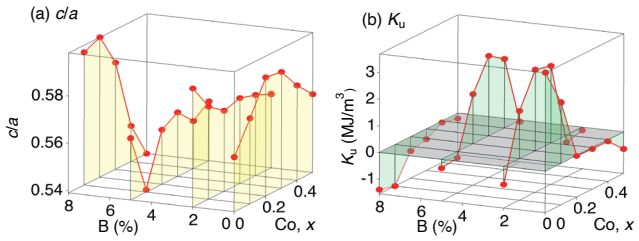


**Fig. 6.** Scatter plot of the axial ratio $c/a$ and the uniaxial magnetic anisotropy constant $K_u$ for $Sm(Fe_{0.95-x}Co_xNi_{0.05})_{12}$-B ($x = 0 \sim 0.5$, B = 0 ~ 8%) thin films.

film ($x$ = 0, B = 0%) with no added B or Co. However, when the Co substitution amount $x$ was 0.5, the $K_u$ value dropped significantly and became negative. However, when 2% and 5% B were added, the $K_u$ value increased with increasing Co substitution, and the easy axis of magnetization became perpendicular. In these B-added films, high $K_u$ values were obtained at Co substitution amount $x$ around 0.2 ~ 0.3. However, as the Co substitution amount $x$ was further increased, $K_u$ decreased. From these results, it was confirmed that positive values of $K_u$ were obtained for films with contents of $x$ = 0 to 0.1 (0%B), 0.1 to 0.3 (2%B), and 0.2 to 0.4 (5%B), and that the $c/a$ values for samples in which the easy axis of magnetization was perpendicular to the film plane were in the range of 0.559 to 0.578. It was also confirmed that when the Co substitution amount was 0.2 ~ 0.5, $c/a$ decreased while $K_u$ increased with increasing the amount of B. Therefore, it is believed that adding B to $Sm(Fe\text{-}Co\text{-}Ni)_{12}$ thin film decreases the $c/a$ and increases $K_u$. However, at 8% B, where the Co substitution amount was $x$ = 0.4 ~ 0.5, the $c/a$ decreased significantly, and $K_u$ also exhibited low values. So, it is thought that the decrease in the $c/a$ contributes to the reduction in $K_u$.

## 4. Conclusion

In this study, $Sm(Fe\text{-}Co)_{12}$ and $Sm(Fe\text{-}Co)_{12}$-B thin films with added Ni, which is expected to stabilize the $ThMn_{12}$-type phase without remarkable decreasing saturation magnetization, were prepared and the variation in the crystal structure and magnetic properties that result from variation of the film composition, such as the amount of Co and Ni substituted for Fe and the amount of B added were also investigated. It was found that the substitution of Co into Fe sites in $Sm(Fe_{1-x-y}Co_xNi_y)_{12}$ thin films elongates the lattice spacing of the $c$-plane, while the substitution of Ni inhibits the formation of the 1:12 phase and instead promotes the formation of $Fe_5Ni$ and α-Fe phases. As the amount of Ni substitution increased, the easy axis of magnetization became predominantly in-plane, but by adding a small amount of B (2% and 5%) and substituting an optimal amount of Co, a composition region in which the easy axis of magnetization was perpendicular was obtained. In other words, it was found that the amount of Co substitution in the $Sm(Fe\text{-}Co\text{-}Ni)_{12}$-B thin film with perpendicular magnetic anisotropy increased with increasing B content. This research will provide valuable insight into the development of next-generation permanent magnets that exhibit high saturation magnetization when the Fe mole fraction is increased.

**Acknowledgements** This work was performed at the Research Institute for Engineering and Technology (High-Tech Research Center) at Tohoku Gakuin University. This work was partially supported by MEXT Program: Data Creation and Utilization-Type Material Research and Development Project (Digital Transformation Initiative Center for Magnetic Materials) Grant Number JPMXP1122715503.

## References

1) Y. Hirayama, Y. K. Takahashi, S. Hirosawa, and K. Hono: *Scr. Mater.*, **138**, 62 (2017).
2) A. M. Gabay and G. C. Hadjipanayis: *Scr. Mater.*, **154**, 284 (2018).
3) P. Tozman, H. Sepehri-Amin, Y. K. Takahashi, and K. Hono: *Acta Mater.*, **153**, 354 (2018).
4) P. Tozman, Y. K. Takahashi, H. Sepehri-Amin, D. Ogawa, S. Hirosawa, and K. Hono: *Acta Mater.*, **178**, 114 (2019).
5) Y. K. Takahashi, H. Sepehri-Amin, and T. Ohkubo: *Adv. Mater.*, **22**, 449 (2021).
6) P. Tozman, H. Sepehri-Amin, and K. Hono: *Scr. Mater.*, **194**, 113686 (2021).
7) H. Sepehri-Amin, Y. Tamazawa, M. Kambayashi, G. Saito, Y. K. Takahashi D. Ogawa, T. Ohkubo, S. Hirosawa, M. Doi, T. Shima, and K. Hono: *Acta Mater.*, **194**, 337 (2020).
8) M. Kambayashi, H. Kato, Y. Mori, M. Doi, and T. Shima: *J. Magn. Soc. Jpn.*, **45**, 66 (2021).
9) A. Bolyachkin, H. Sepehri-Amin, M. Kanbayashi, Y. Mori, T. Ohkubo, Y. K. Takahashi, T. Shima, and K. Hono: *Acta Mater.*, **227**, 117716 (2022).
10) Y. Mori, S. Nakatsuka, S. Hatanaka, M. Doi, and T. Shima: *J. Magn. Soc. Jpn.*, **48**, 17 (2024).
11) H. Sepehri-Amin, N. Kulesh, Y. Mori, T. Ohkubo, K. Hono, and T. Shima: *Scr. Mater.*, **242**, 115955 (2024).
12) X. C. Kou, T. S. Zhao, R. Grössinger, H. R. Kirchmayr, X. Li, and F. R. de Boer: *Phys. Rev. B*, **47**, 3231 (1993).
13) M. Artigas, C. Piquer, J. Rubin, and J. Bartolome: *J. Magn. Magn. Mater.*, **196**, 653 (1999).
14) I. Dirba, J. Li, H. Sepehri-Amin, T. Ohkubo, T. Schrefl, and K. Hono: *J. Alloys Compd.*, **804**, 155 (2019).
15) A. Landa, P. Söderlind, E. E. Moore, and A. Perron: *Appl. Sci.*, **12**, 4860 (2022).
16) A. Landa, P. Söderlind, E. E. Moore, and A. Perron: *Metals*, **14**, 59 (2024).

**Received Oct. 21, 2024; Revised Dec. 12, 2024; Accepted Jan. 17, 2025**

## Editorial Committee Members・Paper Committee Members



### Notice for Photocopying



## 編集委員・論文委員



### 複写をされる方へ



**Journal of the Magnetics Society of Japan**

Vol. 49 No. 3 (通巻第 339号) 2025年5月1日発行

Vol. 49 No. 3 Published May 1, 2025
by the Magnetics Society of Japan
Tokyo YWCA building Rm207, 1–8–11 Kanda surugadai, Chiyoda-ku, Tokyo 101–0062
Tel. +81–3–5281–0106 Fax. +81–3–5281–0107

Printed by JPC Co., Ltd.
Sports Plaza building 401, 2–4–3, Shinkamata Ota-ku, Tokyo 144–0054
Advertising agency: Kagaku Gijutsu-sha

**発行**：(公社)日本磁気学会 101–0062 東京都千代田区神田駿河台 1–8–11 東京YWCA会館 207 号室
**製作**：ジェイピーシー 144–0054 東京都大田区新蒲田 2–4–3 スポーツプラザビル401 Tel.（03）6715–7915
**広告取扱い**：科学技術社 111–0052 東京都台東区柳橋 2–10–8 武田ビル 4F Tel.（03）5809–1132